JGR Atmospheres

RESEARCH ARTICLE
10.1029/2022JD036970

Observed and Parameterized Roughness Lengths for Momentum and Heat Over Rough Ice Surfaces

Maurice van Tiggelen[1], Paul C. J. P. Smeets[1], Carleen H. Reijmer[1], Michiel R. van den Broeke[1], Dirk van As[2], Jason E. Box[2], and Robert S. Fausto[2]

[1]Institute for Marine and Atmospheric Research Utrecht (IMAU), Utrecht University, Utrecht, The Netherlands, [2]Geological Survey of Denmark and Greenland (GEUS), Copenhagen, Denmark

Key Points:

- Observed roughness lengths for momentum over rough ice surfaces are accurately parameterized using snow depth and melting rate
- The parameterization of the roughness length for heat over melting rough ice is updated based on 14 eddy covariance data sets
- Improving the roughness length parameterization improves both the modeled turbulent heat fluxes and the modeled ice ablation

Correspondence to:
M. van Tiggelen,
m.vantiggelen@uu.nl

Citation:
van Tiggelen, M., Smeets, P. C. J. P., Reijmer, C. H., van den Broeke, M. R., van As, D., Box, J. E., & Fausto, R. S. (2023). Observed and parameterized roughness lengths for momentum and heat over rough ice surfaces. *Journal of Geophysical Research: Atmospheres*, *128*, e2022JD036970. https://doi.org/10.1029/2022JD036970

Received 19 APR 2022
Accepted 3 JAN 2023

Abstract Turbulent heat fluxes, that is, the sensible heat flux and latent heat flux, are important sources/sinks of energy for surface melt over glaciers and ice sheets. Therefore, credible simulations of for example, future Greenland Ice Sheet mass loss need an accurate description of these fluxes. However, the parameterization of surface turbulent heat fluxes in climate models requires knowledge about the surface roughness lengths for momentum, heat and moisture, which are currently either unknown or tuned to indirect observations. In this study we take advantage of a large data set of eddy covariance observations acquired during multiple years and at multiple sites over the Greenland Ice Sheet. These in-situ observations are used to develop an improved parameterization for the roughness length for momentum, and update the parameterization for the roughness lengths for heat and moisture over rough ice surfaces. The newly derived parameterizations are implemented in a surface energy balance model that is used to compute surface melt. Sensitivity experiments confirm the high sensitivity of surface melt to the chosen roughness length models. The new parameterization models the sensible heat flux to within 10 W m^{-2}, and the cumulative ice ablation within 10% at three out of four sites. Two case studies demonstrate the important contribution of the turbulent heat fluxes to surface ablation. The presented roughness parameterizations can be implemented in climate models to improve the physical representation of surface roughness over rough snow and ice surfaces, which is expected to improve the modeled turbulent heat fluxes and thus surface melt.

Plain Language Summary Accurately modeling the surface melt over glaciers and ice sheets requires accurately modeling the turbulent heat fluxes between the surface and the atmosphere, which in turn requires a description of the surface aerodynamic roughness. The surface aerodynamic roughness is poorly known, especially in remote areas such as the Greenland ice sheet. In this study we present a large data set of turbulent flux measurements acquired over rough melting ice over the Greenland Ice Sheet and in Iceland. This unique data set is used to develop an improved model for surface roughness lengths of rough ice. We then compute surface melt at different sites on the Greenland Ice Sheet between 2016 and 2021 with a surface energy balance model that includes these newly derived formulations. We find that realistically representing the variations in ice surface roughness leads to a more accurate representation of turbulent heat fluxes, and therefore surface melt. The importance of accurately modeling the turbulent heat fluxes is highlighted further during two cases of extreme melt events. The findings of this study can be used in energy balance models and climate models to improve simulations of surface melt.

1. Introduction

The Greenland ice sheet (hereafter, the ice sheet) is a major contributor to contemporary sea level-rise (IMBIE, 2020), and is expected to contribute further during the next century (Goelzer et al., 2020). The recent increase in the ice sheet's mass loss is for an important part caused by a decrease in surface mass balance (SMB), which is explained by an increase in surface melt and subsequent runoff (Hanna et al., 2021; Mankoff et al., 2021; Van den Broeke et al., 2016). Surface melt is known to be correlated to the large-scale atmospheric circulation (Huai et al., 2020; Mattingly et al., 2020). Yet, state-of-the-art regional climate models (RCMs) still show considerable differences in modeled melt in the ablation area (Fettweis et al., 2020), the area where the surface mass balance is negative and bare ice is at the surface during the melting season. In the ablation area, both the interdiurnal and interannual variability in surface melt are strongly influenced by the turbulent exchange of sensible and latent heat at the surface, that is, the sensible heat flux (SHF) and latent heat flux (LHF) (Van den Broeke et al., 2011; Wang et al., 2021).

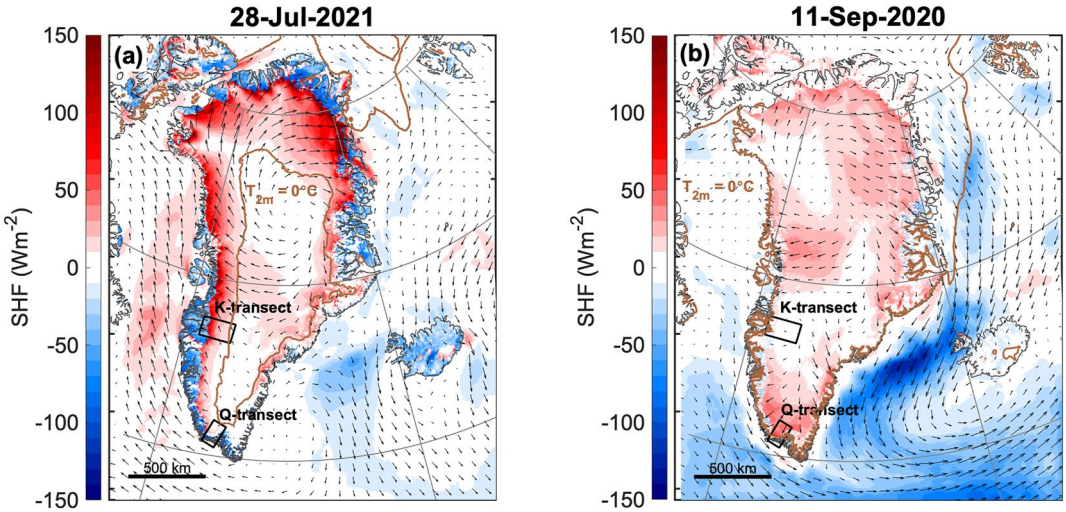

Figure 1. Daily averaged modeled SHF on 28 July 2021 (a) and on 11 September 2020 (b) using the regional climate model RACMO2.3p2, with the 10-m wind vectors and 0°C isotherm of 2-m air temperature. The locations of the K-transect and of the Q-transect are shown. Site QAS_L is on the Q-transect, and sites S5, KAN_L/SHR and S6 are on the K-transect. Both case studies are investigated further in Section 4.1.

Short-lived heat waves can cause anomalous surface melt through turbulent heat fluxes (Fausto et al., 2016). Such an extreme melt event is illustrated in Figure 1a showing modeled SHF from the regional climate model RACMO2.3p2 on 28 July 2021 (Noël et al., 2019). On this day, daily averaged SHF peaked with values up to 150 W m^{-2} over many parts of the ablation area, including the K-transect, a transect of mass balance observations and weather stations located on the western margin of the ice sheet. On this day, the near-surface air temperature was above the melting point hence the SHF was directed toward the surface and contributed to surface melt. A different situation (Figure 1b) occurred on 11 September 2020. At this time, large scale conditions led to a daily averaged SHF reaching 100 W m^{-2} over the Q-transect, which is a similar transect of surface observations located on the southern part of the ice sheet. However, sub-zero near-surface air temperatures that are typical for this time of year mean that the SHF heated the surface, but did not contribute to melt, which was zero. Consequently, accurate simulations of future Greenland Ice Sheet mass loss require an accurate representation of the turbulent heat fluxes, during a variety of large scale atmospheric conditions. Both these case studies will be investigated in more detail using in-situ observations in Section 4.2.

The focus of this study is on contemporary Greenland Ice Sheet SHF, how it is observed in-situ and calculated in surface energy balance (SEB) and RCM applications. In atmospheric models, the surface turbulent heat fluxes are virtually always parameterized using a bulk turbulence model that relies on knowledge of the roughness lengths for heat, moisture and momentum (Moene & van Dam, 2014). These roughness lengths determine the vertical transport of heat, moisture and momentum at the surface through turbulent diffusion, and as such influence the calculation of melt energy over the ice sheet (Braithwaite, 1995; Herzfeld et al., 2006). The roughness lengths are not well known over the ice sheet, therefore constant values for the roughness length for momentum (z_{0m}) are used in most models. While it is known that z_{0m} for ice and snow can vary over two orders of magnitude in both time and space due to changing surface conditions (Brock et al., 2006; Fitzpatrick et al., 2019; Smeets & Van den Broeke, 2008a; Smith et al., 2016; Van Tiggelen et al., 2021), a practical parameterization of z_{0m} over the ice sheet is still lacking. The roughness length for heat (z_{0h}) is commonly set as a constant fraction of z_{0m}. In reality, the fraction z_{0h}/z_{0m} for ice/snow is expected to decrease with increasing roughness Reynolds number, that is, with the turbulent intensity of the flow (Andreas, 1986; Elvidge et al., 2021; Guo et al., 2011; Sicart et al., 2014; Smeets & Van den Broeke, 2008b). The common reason for these simplifications is that direct observations of z_{0m}, z_{0h} and SHF, and therefore the verification of such relationships, are scarce over the ice sheet.

In this study we present a unique data set of eddy-covariance measurements collected in the ablation area of the Greenland Ice Sheet at four different locations during different time periods. We combine these new measurements with previously published eddy covariance measurements taken over rough melting ice, in order to develop improved parameterizations for both z_{0m} and z_{0h}. In Section 2 we describe the observations and the

SEB model used in this study. In Section 3, we further develop the work of Smeets and Van den Broeke (2008a, 2008b), Van Tiggelen et al. (2021), where we present a new simple parameterization for the variation in height of ice hummocks, and an updated parameterization for z_{0h}. In Section 4.1 we perform sensitivity tests with the SEB model over a 5 year period (2016–2021), and present the first evaluation of modeled SHF over several rough, melting ice sites on the ice sheet using direct eddy covariance observations. Finally we compare the new SEB model output to a data set of observations, including melt, during two cases studies in Section 4.2.

2. Methods

2.1. Theory

When a snow or ice surface is at the melting point, the energy available for melt (M) is determined by the surface energy balance:

$$M = R_{net} + SHF + LHF + G, \tag{1}$$

with R_{net} the net absorbed radiation by the surface, SHF the turbulent sensible heat flux, LHF the turbulent latent heat flux and G the subsurface conductive heat flux, all expressed positive when directed toward the surface in W m^{-2}. The SHF and LHF are defined as the net turbulent transfer of sensible and latent heat from the atmosphere to the surface:

$$\begin{aligned} SHF &= -\rho_a C_p \overline{w'T'}, \\ LHF &= -\rho_a L_{e,s} \overline{w'q'}, \end{aligned} \tag{2}$$

with ρ_a the air density, $C_p = 1004$ J kg^{-1} K^{-1} the dry air specific heat capacity, $L_{e,s}$ the latent heat for either evaporation (L_e) or sublimation (L_s), w' the turbulent fluctuations of vertical air velocity, T' the turbulent fluctuations of air temperature and q' the turbulent fluctuations of specific humidity. The overbar denotes time averaging. When the sampling rate of the observations is not high enough to capture all near-surface turbulence, or when near-surface turbulence is not explicitly captured in a model (e.g., in RCMs), the surface turbulent heat fluxes are commonly approximated using the time averaged vertical gradients by invoking Monin-Obukhov similarity theory:

$$\begin{aligned} \overline{w'T'} &= -\left(\frac{\kappa u(z)}{\ln\left(\frac{z}{z_{0m}}\right) - \Psi_m\left(\frac{z}{L}\right) + \Psi_m\left(\frac{z_{0m}}{L}\right)}\right)\left(\frac{\kappa(T(z) - T_s)}{\ln\left(\frac{z}{z_{0h}}\right) - \Psi_h\left(\frac{z}{L}\right) + \Psi_h\left(\frac{z_{0h}}{L}\right)}\right), \\ \overline{w'q'} &= -\left(\frac{\kappa u(z)}{\ln\left(\frac{z}{z_{0m}}\right) - \Psi_m\left(\frac{z}{L}\right) + \Psi_m\left(\frac{z_{0m}}{L}\right)}\right)\left(\frac{\kappa(q(z) - q_s)}{\ln\left(\frac{z}{z_{0q}}\right) - \Psi_q\left(\frac{z}{L}\right) + \Psi_q\left(\frac{z_{0q}}{L}\right)}\right), \end{aligned} \tag{3}$$

in which $u(z)$, $T(z)$, and $q(z)$ are the time averaged horizontal wind speed, air temperature and specific humidity at a height z above the surface, respectively, T_s is the surface temperature and q_s is the surface specific humidity which is assumed at saturation. Ψ_m, Ψ_h, and Ψ_q are the vertically integrated stability functions for momentum, heat and moisture, that we take from Holtslag and De Bruin (1988), L is the Obukhov length and $\kappa = 0.4$ the Von Kármán constant. z_{0m}, z_{0h}, and z_{0q} are the roughness lengths for momentum, heat and moisture, which are defined as the heights above the surface where the logarithmic vertical profile of wind speed, temperature and specific humidity extrapolate to their surface values, respectively. The two terms $\Psi\left(\frac{z_0}{L}\right)$ are small compared to $\Psi\left(\frac{z}{L}\right)$ so we set them to 0. We assume that $\Psi_q = \Psi_h$ and that $z_{0q} = z_{0h}$. The validity of Monin-Obukov similarity over rough, melting ice has been challenged over mountain glaciers by the eddy covariance observations of for example, Conway and Cullen (2013) and Radic et al. (2017). However, no direct evaluation of SHF has so far been performed over the margin of the ice sheet. In this study we assume that Monin-Obukhov similarity is valid, which allows us to estimate the roughness lengths using the measured fluxes and vertical gradients according to:

$$z_{0h} \simeq \frac{z}{\exp\left(\kappa \frac{T(z) - T_s}{T_*} + \Psi_h\left(\frac{z}{L}\right)\right)} \tag{4}$$

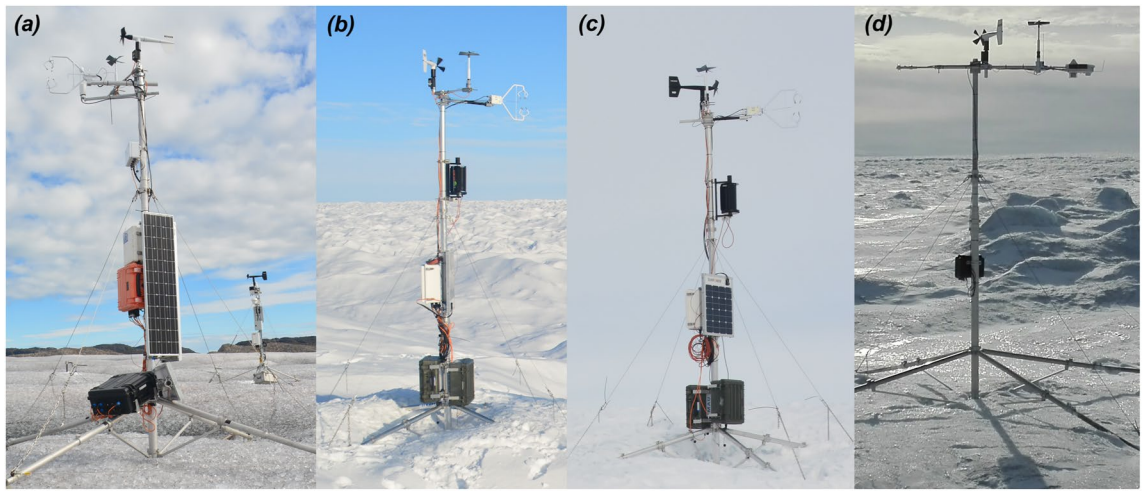

Figure 2. Eddy-covariance stations at (a) QAS_L (b) S5 (c) SHR, and (d) S6. In (a), (b), and (c), both a SEC and VPEC system were operated. In (d) only a VPEC system was installed.

$$z_{0m} \simeq \frac{z}{\exp\left(\kappa \frac{u(z)}{u_*} + \Psi_m\left(\frac{z}{L}\right)\right)} \tag{5}$$

where $u_* = \left(\overline{u'w'}^2 + \overline{v'w'}^2\right)^{1/4}$ is the friction velocity and $T_* = -\overline{w'T'}/u_*$ is the turbulent temperature scale, with u' and v' the turbulent fluctuations of the two components of horizontal wind speed.

2.2. Observations

2.2.1. Automatic weather stations (2016–2021)

Near-surface meteorological and turbulence observations were performed at four sites (Figures 1 and 2). QAS_L is the lowest site of the Q-transect on the southern Greenland Ice Sheet (Hermann et al., 2018), while S5, SHR/KAN_L, and S6 are located in the lower ablation area along the K-transect on the western Greenland Ice Sheet (Smeets et al., 2018). At each site, an automatic weather station (AWS) continuously records 30 min averages of wind speed, wind direction, the four broadband radiation components, air temperature, air relative humidity, air pressure and surface height change during the study period (September 2016–August 2021). Additional details concerning the AWS data and underlying corrections are given by Smeets et al. (2018) for sites S5 and S6, which are part of the IMAU AWS network, and by Fausto et al. (2021) for sites KAN_L and QAS_L, which are part of the PROMICE AWS network. The data include the corrections for incoming direct shortwave radiation for station tilt, the heating of the unventilated air temperature, humidity and longwave radiation sensors, but also the correction of the longwave radiation sensors for the internal sensor temperature and the calibration of the relative humidity sensors with respect to the ice saturation humidity. Different instruments were used to measure the daily ice ablation in addition to the yearly stake measurements: an ablation draw-wire (ADW), a pressure transducer assembly (PTA) or a sonic height ranger mounted on fixed stakes (SR). Details of the ice ablation instruments at each station are given in Appendix A, together with the exact location of each site.

At sites S5 and SHR/KAN_L, the sensor's height above the surface relevant for turbulent flux calculations is not well defined due to the presence of ice hummocks (Figures 2b and 2c). The AWS are typically located on top of an ice hummock, therefore we convert the height of the instruments above the local surface to the true height relevant for the turbulent flux calculations (z in Equation 3) according to Van Tiggelen et al. (2020):

$$z = z_m + H - d, \tag{6}$$

with z_m the height of the sensors above the local surface, H the a-priori assumed average height of the hummocks above the surrounding topography and d the displacement height, which is the reference height above the surface relevant for the flux calculations (Jackson, 1981). Both H and d have a seasonal variability over the ice sheet due to changing surface conditions, but we assume that this seasonal variability in surface conditions only has

an influence on the turbulent flux calculations through changes in z_{0m}, as will be shown in Section 3.1. For S5 and SHR/KAN_L we assume $H = 1$ m and $d = 0.3$ m to process the AWS and eddy covariance measurements.

2.2.2. Eddy covariance stations

At QAS_L, S5 and SHR, sonic eddy covariance (SEC) systems were installed in September 2019 on a separate mast with a CSAT3 instrument (Campbell Scientific) at 3.9 m height at QAS_L and a CSAT3B instrument (Campbell Scientific) at 3.5 m above the local surface at S5 and SHR (Figure 2). The instruments were installed such that the transducer heads point toward the prevailing katabatic wind direction, in order to mitigate for the flow distortion by the instruments as much as possible. The SEC system samples all three wind speed components and air temperature at a rate of 10 Hz, and records the 30-min averages and covariances including $\overline{w'T'}$, $\overline{u'w'}$ and $\overline{v'w'}$. At the same height, air temperature is sampled at 10 Hz with a fine-wire thermocouple (FW3, Campbell scientific). All three masts were also equipped with a vertical propeller eddy covariance (VPEC) system which records the same variables at a rate of 5 Hz (Van Tiggelen et al., 2020). An additional VPEC system was also installed on the AWS mast since September 2016 at sites S5 and S6 that samples at a rate of 0.25 Hz. In addition, we use 2012 SEC data from site S10 (K-transect) from Lenaerts et al. (2014), and 2004 SEC data from S6 and 1996 SEC data from the Vatnajökull icecap (Iceland, Smeets & Van den Broeke, 2008a). These data are complemented with previously unpublished CSAT3 data from site S5 collected during 2006 and 2008. At QAS_L, the SEC system was complemented with an open path gas analyzer (LI-7500, LI-COR) in September 2020 that samples the H_2O concentration at 10 Hz. Some SEC systems were not sampling continuously in order to save power. In total, we use 12 different SEC data sets and two different VPEC data sets recorded at seven different locations between 1996 and 2021. An overview of all the available eddy covariance data is given in Appendix A.

The 30-min averages and covariances are rotated in the average flow direction and tilt corrected using a pitch and a yaw rotation. In addition, we remove the influence of humidity on the SHF as measured with a sonic anemometer using the method from Schotanus et al. (1983) with AWS data. We correct for lateral sensor separation and sampling time-lags using the method described in Moore (1986). The 1996 eddy covariance data from Iceland are also corrected for cross-wind using the method described by Schotanus et al. (1983), since an older type of sonic anemometer was used. Finally, for the VPEC data we apply the sensor response time corrections as described by Van Tiggelen et al. (2020). For the CSAT3 data, we apply a transducer shadowing correction on the 30-min averaged data based on Horst et al. (2015, their Figure 6). For the LI-7500 data we correct for air density fluctuations in the measurement volume using the correction from Webb et al. (1980).

The following data selection criteria are applied to the 30-min averaged eddy covariance data. First, we minimize the uncertainty in the stability corrections by selecting near-neutral runs ($0 < z/L < 0.2$) and we remove data with a low signal-to-noise ratio using the criteria $u_* > 0.1$ m s^{-1}, $u > 3$ m s^{-1} and $|\mathrm{SHF}| > 20$ W m^{-2}. We remove non-stationary runs by requiring $\partial T/\partial t < 0.6$ K hr^{-1} and $\partial u/\partial t < 2$ m s^{-1} hr^{-1}. We mitigate for possible flow distortion by requiring that $|\overline{v'w'}/\overline{u'w'}| < 0.5$ and $1.1 < \sqrt{\overline{w'^2}}/u_* < 1.5$, and by only selecting wind directions that lie within $\pm 45°$ of the orientation of the transducer heads. We remove runs affected by noise by requiring that $u_* < 1.5$ m s^{-1}. The latter value was found to be an optimal threshold to remove runs affected by solid precipitation or blowing snow. For the VPEC data we remove the short gaps due to stalling or freezing of the vertical propeller by selecting runs that verify $\sqrt{\overline{w'^2}} > 0.5$ m s^{-1}. Finally, when computing z_{0h} for all sites except for S10, we remove the uncertainty in determining T_s by only selecting data taken above a melting surface, that is, $T(z) > 275.15$ K, and set the surface temperature to $T_s = 273.15$ K. For the highest site S10 we require $T(z) > 260$ K and compute T_s from the outgoing longwave radiation, otherwise too few data would remain. The amount of data after applying these criteria is significantly reduced (Appendix A), but minimizes the instrumental uncertainties.

2.3. SEB Model

The SEB model used in this study is a further developed version of the model used by Reijmer et al. (1999), Kuipers Munneke et al. (2018), Jakobs et al. (2019), and Huai et al. (2020). The model calculates snow melt and ice ablation by closing the SEB (Equation 1). We force the model with 30-min average AWS observations, from 15 September 2016 until 9 August 2021. To compute the turbulent heat fluxes, Monin-Obukhov similarity is assumed (Equation 3). The latter requires a value for the roughness lengths z_{0m} and z_{0h}, which are either set as constants or parameterized using the new equations derived in the following section. A 24 hr moving

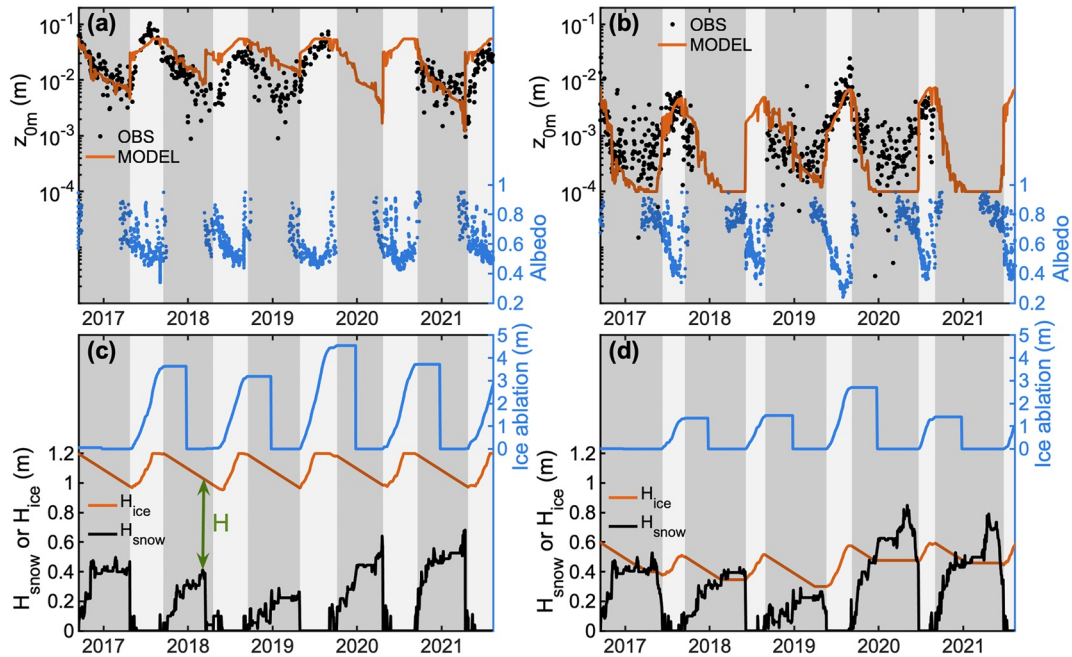

Figure 3. Top panels: S5 (left, a) and S6 (right, b): daily averaged z_{0m} estimated from observations in a fixed wind direction interval (black dots), modeled z_{0m} using the new parameterization from this study (orange line), and measured daily averaged albedo (blue dots). Bottom panels: S5 (left, c) and S6 (right, d): measured daily snow depth (black line), seasonal ice ablation (blue line) and modeled ice roughness height H_{ice} (orange line). The shaded areas denote time periods when no ice ablation is recorded by the draw wire. The green arrow in (c) denotes the modeled height of the obstacles (H).

average albedo is used to compute downward shortwave radiation based on the measured upward shortwave radiation (Van den Broeke et al., 2004). Downward longwave radiation is prescribed from observations, while upward longwave radiation is computed using the calculated surface temperature and assuming emissivity = 1. The latter was chosen to match the measured upward longwave radiation over a melting surface. The surface temperature (T_s) is computed by iteration, then the excess energy is defined as M, and is used for melting either snow or ice.

The SEB model includes a subsurface routine to calculate the conductive heat flux G. The model computes diffusive heat transfer up to a depth of 25 m, with a variable amount of layers of 0.01 m thickness near the surface increasing to 2 m at the bottom. At the bottom we assume that the temperature is unaffected by the air temperature fluctuations in these 5 years simulations, thus we set a zero heat flux. The subsurface temperature is initialized on 15 September 2016 across the whole column with the measured, multi-year average air temperature at each site. Subsurface penetration of shortwave radiation in the ice/snow layers is not taken into account. The latter is known to cause significant internal melt at these locations (Van den Broeke et al., 2008), yet we assume that the total melt energy always interacts at the top layer. The snow has a fixed density of 400 kg m^{-3}, and the snow depth measured by a sonic height ranger is prescribed in the model, and assumed to be zero as soon as ice ablation is recorded by the AWS, in order to accurately represent the start of the ice ablation season.

3. Parameterization of Roughness Lengths

3.1. Roughness Length for Momentum z_{0m}

Figure 3 shows the daily averaged z_{0m} at sites S5 and S6 between 2016 and 2021. These values are calculated from VPEC observations using Equation 5, and selecting only data within 20° of the prevailing katabatic wind direction. Outside these wind directions, the time-averaged z_{0m} can vary by one order of magnitude (Van Tiggelen et al., 2020). At S5, the z_{0m} values range between $\approx 6 \times 10^{-3}$ m before the start of the ablation season to $\approx 2 \times 10^{-2}$ m at the end of the ablation season, which is consistent with previous studies at this location (Smeets & Van den Broeke, 2008a; Van Tiggelen et al., 2021). At the higher location S6, the same strong seasonal cycle is present but z_{0m} values are lower and do not exceed $\approx 5 \times 10^{-3}$ m.

Based on previous drag modeling work (Raupach, 1992; Van Tiggelen et al., 2021), z_{0m} is known to directly depend on both the average height of the roughness obstacles after high-pass filtering of the topography (H_{mod}), and on the obstacle frontal area index (λ). If we consider the obstacles along a fixed wind fetch direction, and we assume that all the obstacles have the same height, then $\lambda = fH_{mod}/100$, with f the number of obstacles per 100 m profile length, and H_{mod} the modeled height of the ice obstacles. As an approximation, we take $f = 8$ obstacles per 100 m, based on UAV surveys over this rough ice area (Van Tiggelen et al., 2021). We then model the total obstacle height as:

$$H_{mod} = H_{ice} - H_{snow}, \tag{7}$$

where H_{ice} is the height of the ice obstacles and H_{snow} is the snow depth, either taken from AWS observations or from RCM output. Note that although they represent the same physical quantity, $H \neq H_{mod}$ since the seasonal cycle in obstacle height is not known a priori. Varying H at site S5 between 1 ± 1 m in Equations 5 and 6 translates in at most a factor 2 difference in estimated z_{0m} from observations, or one order of magnitude less than the observed seasonal cycle in z_{0m} (Figure 3). Snowfall is assumed to fill in the depressions of the topography, which effectively reduces the apparent height of the obstacles seen by the wind. The latter is confirmed when visiting the stations during the accumulation season. H_{ice} is bounded according to $H_{\max}/2 < H_{ice} < H_{\max}$ where $H_{\max}$ is the prescribed maximum height of the obstacles observed at the end of the ablation season, for a particular wind direction. H_{ice} increases during the ablation season due to differential melting and decreases during the accumulation season due to differential sublimation, only when the ice obstacles are not completely buried by snow, that is,:

$$\Delta H_{ice} = \begin{cases} \Delta H_{melt} + \Delta H_{subl} & \text{if } H_{snow} < H_{ice}, \\ 0 & \text{otherwise.} \end{cases} \tag{8}$$

where ΔH_{ice} is used to compute the new ice obstacle height in the next time-step according to:

$$H_{ice,i+1} = H_{ice,i} + \Delta H_{ice}, \tag{9}$$

where i is the current time-step iteration. We model the increase in ice obstacle height during each time-step as:

$$\Delta H_{melt} = K_m M_{melt}, \tag{10}$$

where M_{melt} is the accumulated ice melt during the same time step in meters, either taken from observations or from model output. The constant was set to $K_m = 0.1$ in order to match the z_{0m} observations during the ablation season. A more precise calibration of K_m would require several repeated surveys of the ice obstacles at a single location using for example, photogrammetry, as in Van Tiggelen et al. (2021). We assume a fixed decrease in ice obstacle height due to sublimation only when there is no melt:

$$\Delta H_{subl} = \begin{cases} K_s \left(\text{mm day}^{-1}\right) & \text{if } M_{melt} = 0, \\ 0 \left(\text{mm day}^{-1}\right) & \text{otherwise.} \end{cases} \tag{11}$$

The quantity K_s is fixed to $K_s = 2$ mm day^{-1}, based on short-term height ranger measurements and time-lapse imagery taken during the accumulation season over bare ice at site S5.

The roughness length for momentum (z_{0m}) is then computed using the simplified drag partitioning model from Raupach (1994):

$$z_{0m} = (H - d)\exp(-\kappa\gamma)\exp\left(\widehat{\Psi_H}\right), \tag{12}$$

with $\widehat{\Psi_H} = 0.193$ the wind profile correction within the roughness sublayer and,

$$\gamma = (C_s + C_d\lambda)^{-0.5}, \tag{13}$$

in which the form drag coefficient (C_d) is adapted from Garbrecht et al. (2002) (see also Van Tiggelen et al. (2021)) according to:

$$C_d = \begin{cases} \frac{1}{2}(0.185 + 0.147H) & \text{if } H \leq 2.5\,\text{m} \\ \frac{1}{2}\left(0.22\log\left(\frac{H}{0.2}\right)\right) & \text{if } H > 2.5\,\text{m}. \end{cases} \quad (14)$$

The skin drag coefficient is modeled as:

$$C_s = \left[{C_{s,10}}^{-0.5} - \frac{1}{\kappa}\left(\ln\left(\frac{10-d}{H-d}\right) - \widehat{\Psi_H}\right)\right]^{-2}, \quad (15)$$

with $C_{s,10} = 1.2071 \times 10^{-3}$ after Van Tiggelen et al. (2021). The displacement height (d) is calculated as:

$$d = H\left(1 - \frac{\left(1 - \exp\left(-(c_1\lambda)^{0.5}\right)\right)}{(c_1\lambda)^{0.5}}\right), \quad (16)$$

with $c_1 = 7.5$.

It must be noted at this point that the model from Raupach (1994) (Equation 12) is only valid for moderate frontal area densities ($\lambda \leq 0.1$), which corresponds to roughness obstacles not higher than 1.25 m when assuming $f = 8$ obstacles per 100 m. For larger obstacles, over-sheltering might become important, which may require more sophisticated models (Shao & Yang, 2008). Furthermore, this model yields an unrealistic value of $z_{0m} = 0$ m when $H = 0$ m. This is overcome by setting a lower limit to H of 0.01 m, which then yields $z_{0m} \approx 10^{-4}$ m.

In summary, the height of the roughness obstacles (H) is determined using ice ablation and snow depth, and by prescribing a constant value for $H_{\max}$ for each location. Then the corresponding z_{0m} values are computed using the steps above. The model results at S5 and S6 are shown in Figure 3, where the only varying parameter across sites is $H_{\max}$. At S5 we set $H_{\max} = 1.2$ m and at S6 we set $H_{\max} = 0.6$ m, based on photographic evidence. The resulting modeled z_{0m} at S5 and S6 during 2016–2021 is shown in Figure 3. The model is able to accurately simulate the yearly z_{0m} cycle at both stations, although differences persist. Interestingly, the logarithmic increase of z_{0m} during summer due to obstacle height increase is coincident with the decrease in albedo due to surface impurities, which is consistent with remote sensing observations (Nolin & Payne, 2007). As such, during a high melt year such as 2019, albedo is lower than usual while z_{0m} is larger than usual, since differential melting is greater. Furthermore, winter z_{0m} value are underestimated at S6 when all the ice obstacles are buried by snow. In contrast, z_{0m} values are overestimated during winter in 2018 and 2019 at S5. This means that additional processes must be considered for a snow surface, such as the development of sastrugi as parameterized by Agosta et al. (2019), or the influence of blowing snow. For a melting snow surface, the development of ablation hollows may also be an important process for z_{0m} (Brock et al., 2006). Nevertheless, the newly developed model better reproduces the seasonal z_{0m} evolution than, for example, using a constant value for snow and ice (Brock et al., 2006).

3.2. Roughness Length for Heat z_{0h}

The ratio of roughness length for heat (z_{0h}) over z_{0m} for all 12 data sets of SEC observations is shown in Figure 4 as function of the roughness Reynolds number $Re_* = u_* z_{0m}/\nu$, where $\nu = \mu/\rho$ is the air kinematic viscosity, ρ the air density and μ the air dynamic viscosity. Both z_{0m} and z_{0h} are estimated from 30-min sonic eddy covariance observations using Equations 4 and 5, and the ratio z_{0h}/z_{0m} is bin-averaged per data set and per month for different logarithmically-spaced Re_* classes.

No clear seasonal relationship is visible (Figures 4a–4f), yet all the data sets confirm that the z_{0h}/z_{0m} ratio strongly decreases for increasing Re_* (Figure 4g). This is a consequence of form drag that increases turbulent momentum transfer at higher Re_* values, whereas turbulent heat transfer is controlled by the much less efficient process of molecular diffusion, which occurs in the very thin viscous layer in direct contact with the surface. However, not all the data sets imply the same z_{0h}/z_{0m} relation versus Re_*. At the smoother surface of sites S6, A4 and QAS_L, the observed z_{0h}/z_{0m} ratio generally agrees with the parameterization of Smeets and Van den Broeke (2008b). At the rougher sites S5, A5 and SHR, the data lie between the model of Andreas (1986) and the parameterization of Smeets and Van den Broeke (2008b). This means that the modeled sensible heat fluxes using the latter parameterization will be larger than the observed fluxes, at least when using the same gradients and z_{0m}. The other models (Brutsaert, 1982; Joffre, 1988; Kanda et al., 2007; Li et al., 2020) also fail to reproduce the observed z_{0h}/z_{0m} for the whole range of Re_*.

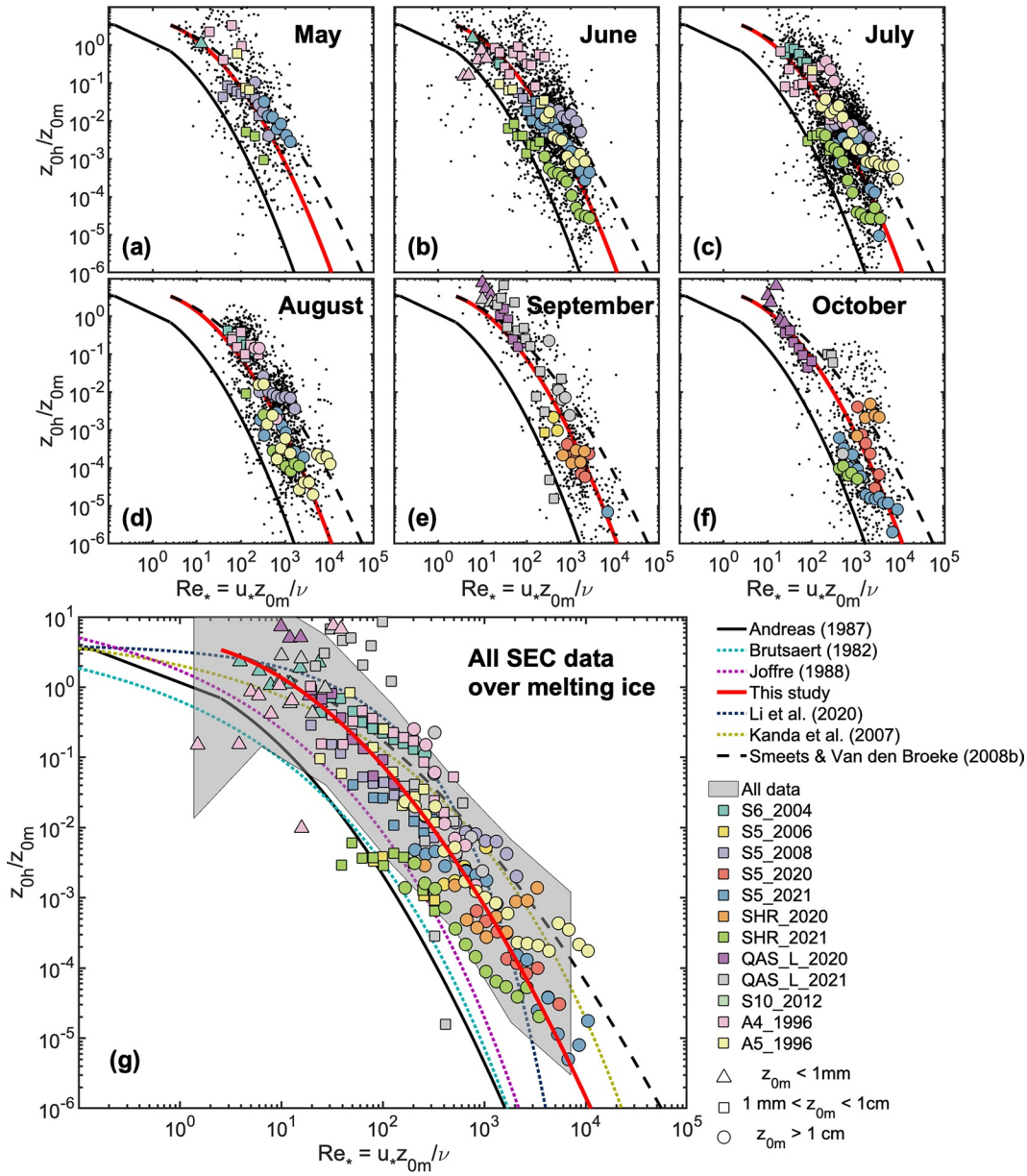

Figure 4. Observed z_{0h}/z_{0m} ratio as function of roughness Reynolds number $Re_* = u_* z_{0m}/\nu$ for 12 sonic eddy covariance data sets acquired over melting snow/ice. Top panels (a–f) separate the data in monthly intervals from May to October, while the bottom panel (g) contains all the data averaged in logarithmically spaced bins. The continuous and dashed lines denote the models from Andreas (1986), Brutsaert (1982), Joffre (1988), Kanda et al. (2007), Smeets and Van den Broeke (2008b), Li et al. (2020), and the updated parameterization (Equation 17). Symbols denote the bin-averaged z_{0m} per data set, and the shaded area in (g) denotes two times the standard deviation of all the data per Re_* bin. The black dots in (a–f) denote all the data used for bin-averaging.

When bin-averaging all the 12 data sets over all time periods, the following new relation best reproduces the observations, which is an adapted version of the model from Andreas (1986):

$$\ln\left(\frac{z_{0h}}{z_{0m}}\right) = b_0 + b_1 \ln(Re_*) + b_2 (\ln(Re_*))^2 \tag{17}$$

with $b_0 = 1.5$, $b_1 = -0.15$, and $b_2 = -0.16$. We propose to use this updated relation for rough snow/ice, that is, $z_{0m} > 10^{-3}$ m. For smooth snow/ice, that is, $z_{0m} \leq 10^{-3}$, the model from Andreas (1986) should be used, as there

are insufficient measurements to verify the new relationship for smooth surfaces. Note that only for lower values of Re_*, the updated relationship resembles the relation from Smeets and Van den Broeke (2008b), which was developed using data from S6, A4 and A5 using a comparable data selection strategy.

As demonstrated by Andreas (2002), plots of z_{0h}/z_{0m} versus $Re_* = u_* z_{0m}/\nu$ from empirical data may suffer from self-correlation due to the shared variable z_{0m} in both axes. Using the equations in Andreas (2002) we computed the expected correlation between z_{0h}/z_{0m} and $Re_* = u_* z_{0m}/\nu$ for all the different data sets used in Figure 4 (Table A2). The largest expected correlation (−0.7183) is found in the S6_2004 data, which is a data set obtained higher up in the ablation area where the surface is relatively smooth and temperature gradients are smaller, leading to a relatively smaller variability in z_{0m}, z_{0h} and SHF. However, the average self-correlation for all data sets is much lower (−0.3237) due to a large spread in z_{0h} values (Table A2). The large spread in z_{0h} values is caused by a larger temporal variability in measured turbulent heat fluxes (T_* in Equation 4), which is typical in the lower part of the ablation area of the ice sheet. Hence, using longer data sets from various locations where large SHF values are observed reduces the problem of artificial correlation (Andreas, 2002).

4. Results

4.1. Sensitivity Tests

In order to test the improved parameterizations for both z_{0m} (Section 3.1, Equation 12) and for z_{0h} (Section 3.2, Equation 17), we run the SEB model for the four sites with two different settings for z_{0m}, and three different settings for z_{0h}, that is, six permutations. For z_{0m}, we either use a constant value $z_{0m} = 1.3 \times 10^{-3}$ m for all sites, or use the parameterization described in Section 3. The maximum height of ice roughness obstacles ($H_{\max}$) is the only varying parameter across sites, and set to 0.5 m, 1.2 m, 1 m and 0.6 m for QAS_L, S5, KAN_L, and S6, respectively. These values are based on photographs taken during the yearly station maintenance at the end of the ablation season. This value is site specific, and should be adapted to each area of interest. An alternative is to estimate $H_{\max}$ using ICESat-2 measurements, or using UAV photogrammetry (Van Tiggelen et al., 2021). For z_{0h}, we test the two different parameterisations from Andreas (1986) and Smeets and Van den Broeke (2008b), in addition to the adjusted parameterization derived in Section 3.2 (Equation 17).

4.1.1. Impact on Modeled SHF

Figure 5 compares daily averaged observed and modeled SHF using the parameterized z_{0m} value. Panels (a) and (b) show the comparison at sites S5 with VPEC data and at QAS_L with SEC data with the updated z_{0h} parameterization as an example. Panel (c) shows the bias and root-mean-square error (RMS) for all the data sets and modeled z_{0m}. While the RMS is still considerable (20.5 W m^{-2} at S5 and 17.2 W m^{-2} a QAS_L), the bias is close to zero and smaller than when the models from Andreas (1986) and Smeets and Van den Broeke (2008b) are used (Figure 5c). The RMS ranges between 7.8 and 25.3 W m^{-2}, compared to a mean SHF during melting days of 42 W m^{-2} at S6 to 89 W m^{-2} at S5. When using the model from Andreas (1986), SHF is underestimated by 10.6 W m^{-2} at SHR, and up to 28 W m^{-2} at S5. On average, the model from Smeets and Van den Broeke (2008b) overestimates the SHF by 4.3 W m^{-2} at S5, to 15.2 W m^{-2} at SHR. The revised z_{0h} model from Equation 17 yields improved SHF for all stations, with a mean bias of 3.2, −4.1, −6.7, and 4.2 W m^{-2} for QAS_L, S5 (VPEC data), S5 (SEC data) and SHR, respectively. At site S6, all the models underestimate the SHF, with a bias between −12.2 and −21.1 W m^{-2}.

Figure 5c also compares average modeled z_{0m} values to the values estimated from in situ observations. At all sites, modeled z_{0m} values are larger than the value (1.3×10^{-3} m) that is typically used over snow or ice, ranging from 7.4×10^{-3} m at S6 to 1.94×10^{-2} m at S5. This means that the modeled SHF using this fixed value for z_{0m} will be smaller than the modeled SHF using the newly parameterized z_{0m}, when using the same model for z_{0h}. Furthermore, the values are also higher than the observations for all sites except at S6. For instance at S5, the average z_{0m} value over the 268 days of selected VPEC data during melting conditions is 4.18×10^{-2} m, versus the observed averaged value of 1.94×10^{-2} m. An optimal set for model parameters (f, K_m, K_s, C_d, C_s, $H_{\max}$) could be used to match the observed z_{0m} at a single site, but this would limit the applicability of the model to sites with eddy covariance observations. Interestingly, using a higher z_{0h} value also results in a larger modeled z_{0m}, since a larger SHF promotes ablation, therefore a faster growth of roughness obstacles during the ablation season (Equation 10). Yet, this effect remains small compared to the difference with the observed values: that is, a modeled z_{0m} value ranging from 4.11×10^{-2} to 4.22×10^{-2} m at S5 (VPEC data) depending on the chosen model for z_{0h} (panel c).

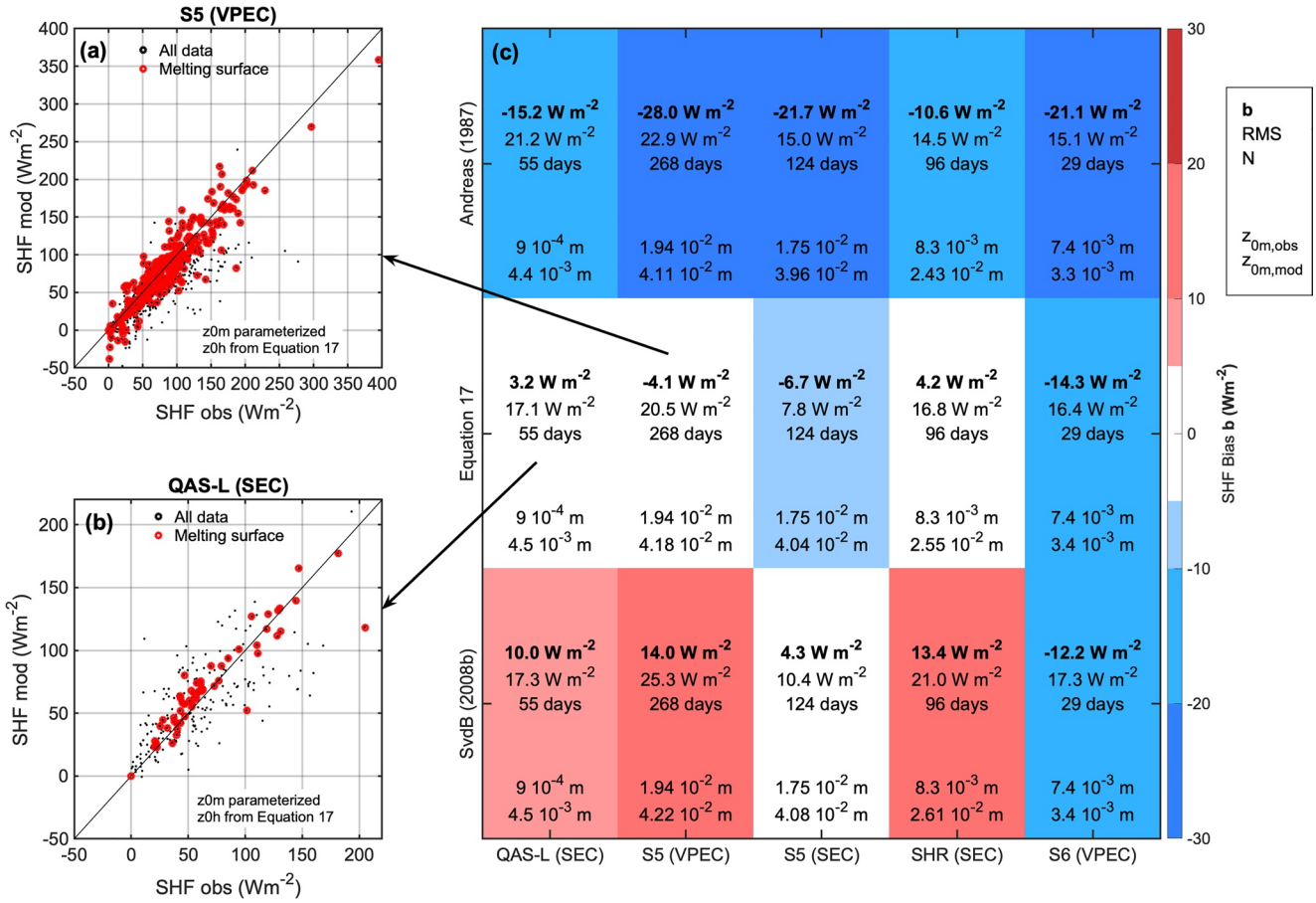

Figure 5. Modeled daily averaged sensible heat flux (SHF) versus sonic eddy covariance (SEC) and vertical propeller eddy covariance (VPEC) observations at four sites. Two different data sets are shown for site S5. Panels (a and b) compare the modeled SHF using a parameterized z_{0m} and z_{0h} from Equation 17 to the observed SHF from eddy covariance observations. Panel (c) contains in each cell from top to bottom: the bias (b), room-mean-square error (RMS), number of observations (N), observed z_{0m}, and modeled z_{0m}. The simulations use a parameterized z_{0m}, and use a parameterized z_{0h} from either Andreas (1986), Equation 17 or Smeets and Van den Broeke (2008b) (different rows). The color in (c) indicates the bias. All z_{0m} values are rounded to 10^{-4} m.

4.1.2. Impact on Modeled Ice Ablation

The total 2016–2021 cumulative ice ablation from the SEB model using six combinations for z_{0m} and z_{0h} for all four AWS sites (QAS_L, S5, KAN_L/SHR, S6) are compared to manual stake observations in Figure 6. We also compare the differences in modeled ablation to the uncertainty in the AWS forcing by perturbing the optimal model run (z_{0m} modeled, z_{0h} from Equation 17, red line) with a broadband albedo change of ±0.02. This uncertainty was quantified as follows. Besides suffering from tilt and window-heating, an unventilated net radiometer reading may contain a so called "zero offset" bias in the shortwave components due to cooling of the instrument body by infrared radiation. For the pyranometer in the CNR4 instrument, the SW_{up} and SW_{down} biases are reported to be less than 15 W m^{-2} by the manufacturer, and linearly depend on the net infrared radiation (Behrens, 2021). The estimated albedo using AWS data is defined:

$$\alpha = \frac{SW_{up} + b}{SW_{down} + b}, \tag{18}$$

with SW_{down} and SW_{up} the true downward and upward shortwave radiation, respectively, and b the bias. Using the maximal reported value for b = 15 W m^{-2}, and SW_{down} = 300 W m^{-2}, SW_{up} = 150 W m^{-2}, which are representative for bare ice during summer over the ice sheet, we find α = 0.524. The latter is 0.024 higher than the true surface albedo SW_{up}/SW_{down} of 0.500. Therefore a bias of ±0.020 in measured albedo was deemed realistic to quantify the propagating error in the SEB model due to radiometer errors.

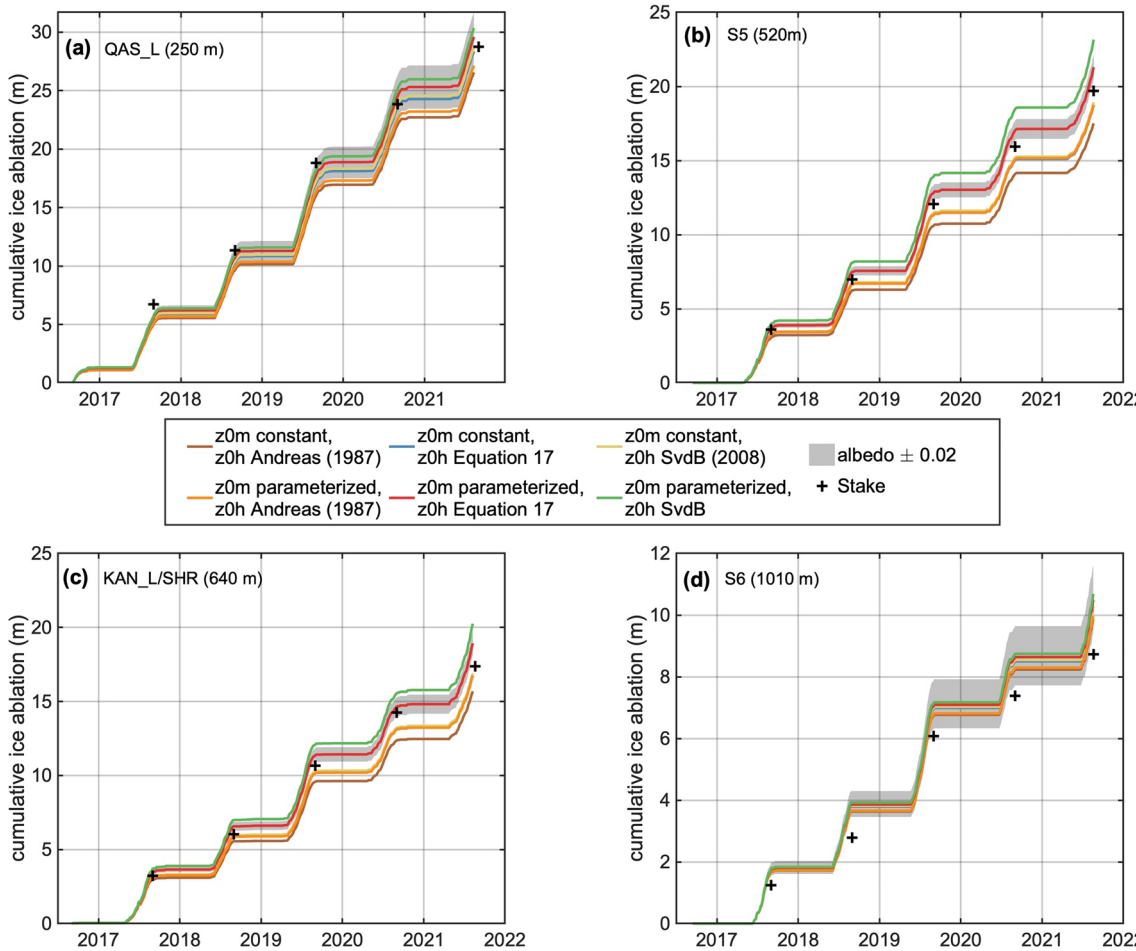

Figure 6. Modeled cumulative ice ablation at four sites on the Greenland Ice Sheet with the surface energy balance (SEB) model using six possible settings for z_{0m} and z_{0h}. The black squares denote the manual, yearly stake observations. The shaded area denotes the range of modeled ice ablation by perturbing the prescribed albedo to the SEB model by a change of ±0.02, for the run with a parameterized z_{0m}, and z_{0h} from Equation 17.

Overall, the optimal run (red line) agrees best with the independent stake observations (within 10%), except at site S6 where ablation is overestimated (+20%). Since the contribution of turbulent heat fluxes to total ablation is smallest at S6 (≈20%, Kuipers Munneke et al. (2018)), using different z_{0m} and z_{0h} models does not explain this bias. Further, SHF and LHF partly compensate each other at this higher elevation near equilibrium line altitude, as demonstrated by Steffen (1995). At the lower sites, different z_{0m} and z_{0h} models considerably affect modeled ablation; for example, up to 1.13 m ice per year at S5, or 29% of the yearly ablation. The modeled z_{0m} and the z_{0h} from Smeets and Van den Broeke (2008b) yields the largest ablation (green line), while a fixed $z_{0m} = 1.3 \times 10^{-3}$ m and the z_{0h} from Andreas (1986) yields the lowest ablation (brown line). The sensitivity of the modeled ablation to the chosen z_{0h} model is largest at S5, which is a low-lying site (520 m) with ice hummocks higher than 1 m, and where the contribution of SHF to melt energy is large. QAS_L is situated at an even lower elevation (280 m), yet the sensitivity to the choice of z_{0h} is less pronounced than at S5 since the average z_{0m} value is smaller. Also, differences between the modeled ablation using a fixed $z_{0m} = 1.3 \times 10^{-3}$ m are smaller; for example, 0.28 m of ice per year at S5, or 7% of the yearly ablation; since all z_{0h} parameterizations are similar at lower roughness Reynolds numbers (Figure 4).

To summarize, the parameterization for z_{0h} should be carefully chosen over areas that are both rough and situated at lower elevations. In these areas, the contribution of SHF to ice ablation is the largest, and z_{0h} models differ most. Both an accurate z_{0m} and z_{0h} model are required to correctly model the SHF, although an underestimated z_{0h} can still partly be compensated by an overestimated z_{0m}. Yet the z_{0m} values also affects the momentum fluxes, thereby impacting the wind field in coupled models. Finally, radiation measurement errors lead to a considerable spread in modeled ablation (25% at S6), especially at higher elevation or darker surface sites where the relative contribution of turbulent fluxes to

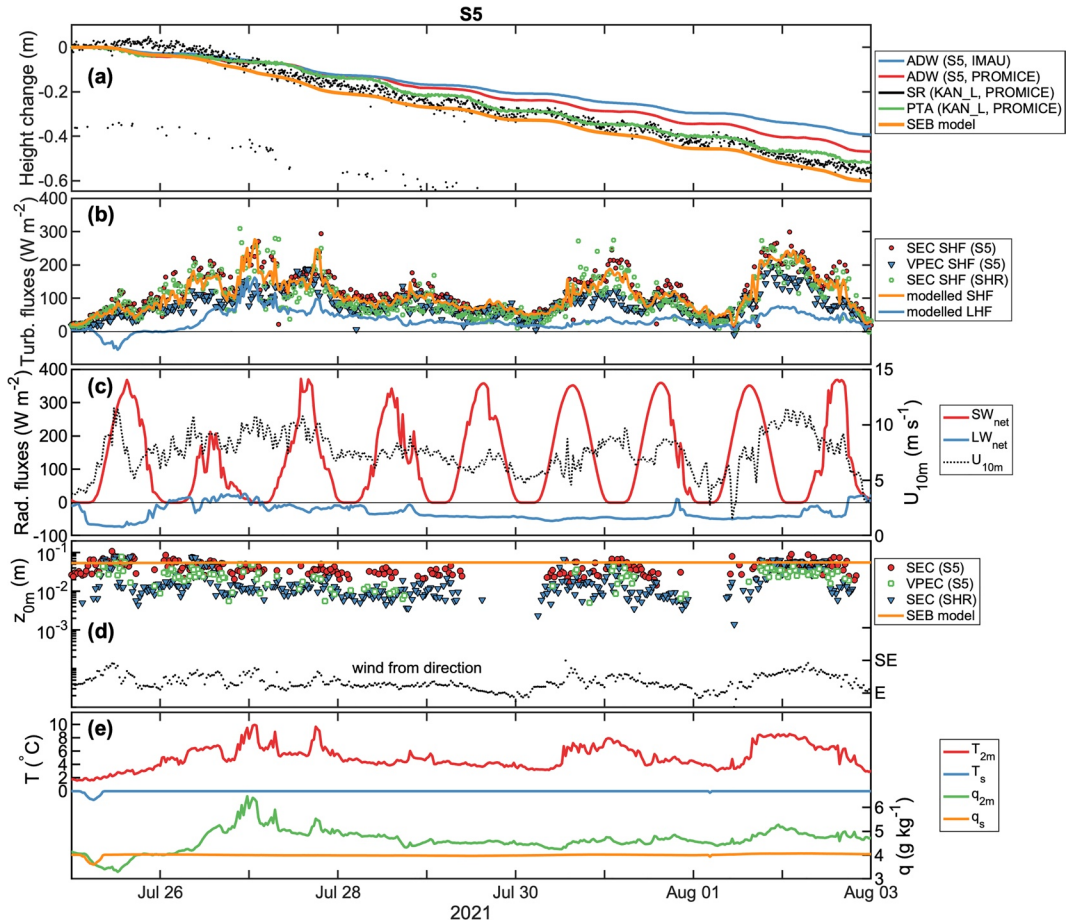

Figure 7. Case study at S5. Top panel (a) includes the modeled height change using the surface energy balance model with a parameterized z_{0m} and z_{0h} from Equation 17, in addition to the surface height change recorded by an ablation draw wire (ADW), sonic height ranger (SR) and pressure transducer assembly (PTA). Panel (b) illustrates the sensible heat flux (SHF) and latent heat flux (LHF) from both model, sonic eddy covariance (SEC) and vertical propeller eddy covariance (VPEC) observations. Panel (c) contains the observed net surface absorbed fluxes of shortwave (SW_{net}), longwave radiation (LW_{net}), and the 10-m wind speeds. Panel (d) contains estimated z_{0m} values from both SEC and VPEC observations, as well as the modeled z_{0m} value and the observed wind from direction. Bottom panel (e) illustrates the 2m air temperature and specific humidity, and both modeled surface temperature and surface specific humidity.

ablation is smaller. We recommend the use of the newly developed z_{0m} model developed in this study with well chosen values for parameters including $H_{\max}$, in combination with the updated parameterization for z_{0h} (Equation 17). The parameters of both the z_{0m} and z_{0h} parameterizations were calibrated with a greatly reduced amount of measurements, due to the strict selection procedure (Appendix A). Yet, the updated parameterizations give the most accurate results when applied in the SEB model forced with 4 years of continuous, meteorological forcing.

4.2. Case Studies: Strong Melt Events

To demonstrate the important short-term variability of SHF and its impact on melt, we selected two cases with important contributions of the SHF to the melt energy. This enables us to evaluate the SEB model with optimal roughness length settings, but also to highlight the impact of instrumental uncertainties in observing ice ablation during extreme melt episodes (Figures 7 and 8). The modeled ground heat flux (G) is not shown, since its contribution to the SEB during melting events is usually negligibly small compared to the other fluxes (Van den Broeke et al., 2008).

4.2.1. S5: 25 July–3 August 2021

At site S5, we analyze the period between 25 July and 3 August 2021, during which an important peak in SHF was observed at S5 and SHR (Figure 7b, dots). This peak is explained by a high (≈10 m s^{-1}) wind speed (Figure 7c),

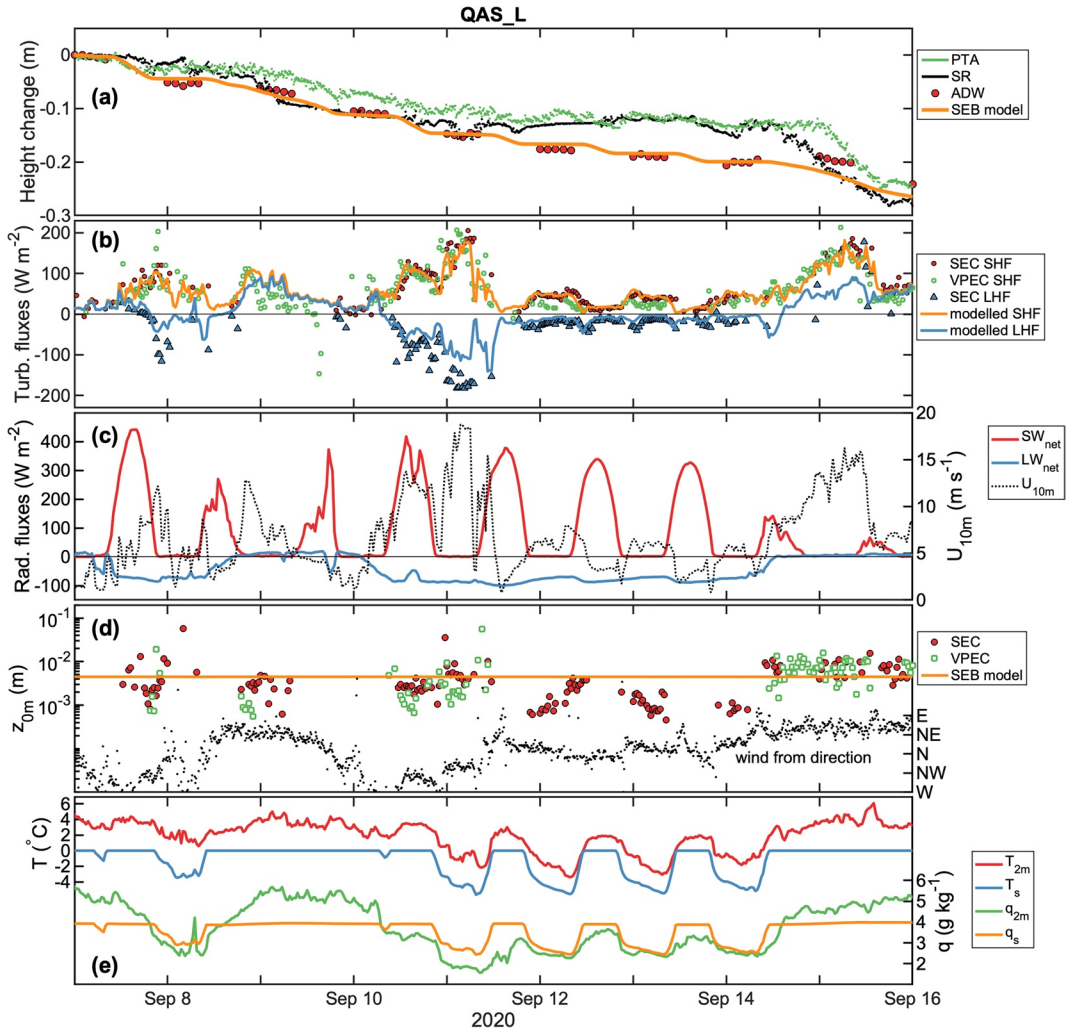

Figure 8. Same as Figure 7 for QAS_L.

and a large ($8°C$) surface to air temperature gradient (Figure 7e). This peak is realistically modeled (orange line, Figure 7b), with accurate representations of both z_{0m} (panel d) and z_{0h} (not shown). In combination with a large net absorbed radiation, the modeled surface lowering during this period is substantial (6.7 cm per day, 60 cm total, panel a). The latter modeled surface lowering agrees well (within 15%) with both the SR and PTA observations from KAN_L (≈5 km upslope, 160 m higher), but does not agree with the two ADW measurements at S5. The mismatch is evidence of the considerable spatial variability in ice ablation during short time periods. We expect the net absorbed radiation and the turbulent heat fluxes to be heterogeneous in the rough area surrounding these weather stations. Besides, the ADW masts at S5 are anchored several cm into the ice surface, making them more sensitive to subsurface melt caused by solar insolation, but not to surface melt caused by turbulent heat fluxes. This is visible in the night between 26 and 27 July in Figure 7a, during which the SEB model and the observations at KAN_L suggest ablation, but both draw wires at S5 do not. Over longer periods, the ADW masts still record the same cumulative ablation since they sink back in the ice during daytime. At this site, the VPEC and SEC observations of SHF and z_{0m} also do not perfectly match. This is likely explained by the different placement of the masts on the ice hummock (10 m apart), in combination with the uncertainty related to the slow-response correction of the VPEC sensors (Van Tiggelen et al., 2020).

4.2.2. QAS_L: 7–16 September 2020

At QAS_L, we analyze the data between 7 and 16 September 2020, during which both SHF and LHF, and all three types of independent ablation measurements are available. We only consider the nighttime data of the ADW, since

daytime internal heating of the logger caused nonphysical values, which was not yet corrected for in this instrument. Overall, the SEB model captures within 3% the 28 cm of ablation that was recorded by all three sensors during this time period (Figure 8a). However, day-to-day differences between the ablation measurements also suggest some spatial variability in melt. The SHF is accurately represented by the SEB model (within 10%), although the upward LHF appears to be underestimated (Figure 8b). Few LHF measurements are available when LHF >0 (downward), since these are often conditions when the air is warm and close to saturation, which negatively affects the measurements with an open path gas analyzer. Furthermore, the thick cloud cover during such conditions (Figure 8c) reduces the power input from the solar panels, which means that the gas analyzer was often switched off to safeguard the batteries. Interestingly, on 10–11 September, the large peak in SHF (Figure 8b), explained by a high ($\approx$15 m s^{-1}) wind speed (Figure 8c), is fully compensated by a negative LHF caused by dry conditions (Figure 8e), which prevents nighttime melt (Figure 8a). On the other hand, on 9 and 16 September, both a positive SHF and LHF enhance nighttime melt. This is confirmed by the PTA and SR measurements, and to a lesser extent by the ADW (Figure 8a). The average z_{0m} during this time period is realistically captured (Figure 8d), although sub-daily changes in z_{0m} linked to changing wind directions are not. For instance, wind directions deviating from the prevailing, northerly katabatic wind direction have slightly larger z_{0m} values, which are not represented in the current z_{0m} model formulation. The latter also holds for the easterly (katabatic) wind direction at S5 (panel d).

5. Conclusions/Summary

Turbulent heat fluxes, that is, the sensible heat flux (SHF) and the latent heat flux (LHF), are important sources/sinks of energy for the Greenland Ice Sheet. Any atmospheric model, ranging from large eddy simulations to earth system models must therefore accurately represent these turbulent fluxes, which demands accurate estimates of the aerodynamic roughness lengths for momentum (z_{0m}) and heat (z_{0h}), provided that similarity theory is applied between the lowest model level and the surface.

In this study we applied a bulk turbulent drag model to model z_{0m} variations in time using information on ice melt and snow depth. We tested this model at four contrasting sites on the ice sheet for which eddy covariance data are available. The model is able to reproduce the observed seasonal cycle in z_{0m} (Figure 3). The z_{0m} values increase during the start of the melting season when the seasonal snow melts, uncovering the rough underlying ice. When the snow is gone, ice hummocks are modeled to gradually increase in height due to differential ablation, which further increases z_{0m} during the ablation season. At the start of the accumulation season, z_{0m} decreases again when the topographic depressions between the ice obstacles are assumed to be gradually filled with fresh snow. The remaining exposed top of the ice hummocks are also modeled to decrease in height due to differential sublimation, which reduces the z_{0m} values further.

Twelve eddy covariance data sets, acquired since 1996 over rough ice and snow surfaces in both Greenland and Iceland, are used to compute z_{0h}. Although the spread between the in situ observations remains large, all data confirm that the z_{0h}/z_{0m} ratio decreases with increasing roughness Reynolds number ($Re_* = u_* z_{0m}/\nu$, Figure 4). A new empirical relationship was fitted (Equation 17), which improves modeled SHF over rough ice (Figure 5), which in turn improves the modeled ice ablation (Figure 6).

The methods described in this study can be used to improve the representation of turbulent heat fluxes over rough ice in either SEB models using AWS data as input, or coupled surface-atmosphere models. The impact of the revised parameterisations for both z_{0m} and z_{0h} was found to be particularly large in the lower part of the ablation area, where the largest vertical gradients of wind speed and temperature are found together with large ice hummocks or crevasses, and where a negative LHF less frequently offsets the SHF. An important uncertainty remains in the representation of the spatial patterns of ice ablation at the scale of the roughness obstacles themselves. Differences between in situ ablation measurements in the same area strongly confirm a spatial variability in surface ablation (Figures 7 and 8). Yet, neither of the current state-of-the-art SEB models nor regional climate models are able to resolve melt at the meters scale, complicating the direct comparison of point in situ observations with large scale models over such complex surfaces.

Appendix A: Data Description and Acronyms

The metadata of all the eddy covariance data sets used in this study are given in Table A1. The acronyms used in this study are summarized in Tables A2 and A3.

Journal of Geophysical Research: Atmospheres
10.1029/2022JD036970

Table A1
Description of Eddy Covariance Data Sets

Site	Location	Time period	Instrument (method)	Valid runs when t_air >2C/valid 30 min runs/total run	z (m)	z_{0m}(m) 10%–90% quantile (t_air > 2C)	SHF (W m^{-2}) 10%–90% quantile (t_air > 2C)	Albedo range	Ablation sensor
QAS_L	61.0305; –46.8497; 250 m	29 August 2019 to 15 February 2020	CSAT3 (SEC)	250/786/5,109	3.75	6 10-4–3.0 10-3	51.9–172.7	0.16–0.81	ADW, PTA, SR, stake
		21 August 2020 to 08 February 2021	CSAT3 + LI-7500 (SEC)	103/596/7,869	3.75	9 10-4–1.11 10-2	53.0–193.6	53.0–193.6	ADW, PTA, SR, stake
S5	67.09431; –50.07208; 520 m	01 September 2005 to 09 March 2006	CSAT3 (SEC)	90/574/4,455	4.52	2.5 10-3–2.32 10-2	46.3–166.2	0.54–0.91	SR, stake
		04 April 2008 to 31 August 2008	CSAT3 (SEC)	1,893/2,329/6,852	4.45	5.6 10-3–4.28 10 -2	37.7–143.9	0.48–0.95	SR, stake
		05 September 2019 to 31 October 2019	CSAT3B (SEC)	313/1,020/2,515	4.45	2.45 10-2–1.102 10-1	42.2–137.9	0.50–0.95	ADW, stake
		11 September 2020 to 09 August 2021	CSAT3B (SEC)	2,418/5,759/11,268	4.45	9.6 10-3–5.96 10-2	44.1–162.9	0.47–0.95	ADW, stake
		15 September 2016 to 31 August 2021	Propellers and thermocouple (VPEC)	1,761/4,821/67,235	4.45	6.3 10-3–5.98 10-2	45.1–182.8	0.45–0.95	ADW, stake
SHR/ KAN_L	67.09674; –49.96082; 640 m	04 September 2019 to 02 December 2019	CSAT3B (SEC)	273/1,493/3,779	4.45	1.29 10-2–6.91 10-2	39.6–122.1	0.43–0.90	PTA, SR, stake
		10 September 2020 to 09 August 2021	CSAT3B (SEC)	1,760/2,973/9,375	4.45	3.9 10-3–5.04 10-2	33.7–113.4	0.41–0.92	PTA, SR, stake
S6	67.07941; –49.40981; 1010 m	01 September 2003 to 18 August 2004	CSAT3 (SEC)	873/4,578/15,656	2.75	5 10-4–1.05 10-2	23.6–73.2	0.45–0.95	SR, stake
		15 September 2016 to 08 September 2020	Propellers and thermocouple (VPEC)	85/1,102/69,311	2.8–3.7	1.3 10-3–7.6 10-3	37.1–124.8	0.24–0.95	ADW, stake
S10	66.9999; –47.0199; 1880 m	13 August 2012 to 24 October 2012	CSAT3 (SEC)	4/30/1,603	3.7–4.2	3 10-5–1 10-4	11.7–20.5	0.58–0.95	SR, stake
A4	64.09083; –16.32889; 279 m	17 May 1996 to 01 September 1996	Solent 1012 R2 (SEC)	844/873/4,379	3–3.65	8 10-4–1.14 10-2	34.4–234.8	–	SR, stake
A5	64.12278; –16.36889; 381 m	19 May 1996 to 31 August 1996	Solent 1012 R2 (SEC)	679/679/4,844	3–4.65	5 10-3–1.221 10-1	30.2–163.1	–	SR, stake

Table A2
Standard Deviation (σ) of Observed $\ln(z_{0m})$, $\ln(z_{0m})$ $\ln(u_*)$, and Estimated Expected (or Fictitious) Correlation (ρ) After Andreas (2002) for All Sonic Eddy Covariance Measurements During Melting Conditions

Data set	$\sigma\ln(z_{0m})$	$\sigma\ln(z_{0h})$	$\sigma\ln(u_*)$	ρ
S6 2004	1.1424	1.0421	0.2751	−0.7183
S5 2006	0.8024	2.0670	0.2531	−0.3451
S5 2008	0.8113	1.5715	0.2945	−0.4312
S5 2020	0.5590	2.7403	0.3471	−0.1698
S5 2021	0.7623	2.7702	0.3696	−0.2388
SHR 2020	0.6268	2.3241	0.3435	−0.2284
SHR 2021	0.9701	2.4093	0.3325	−0.3533
QAS_L 2020	0.8165	2.0782	0.2981	−0.3435
QAS_L 2021	0.9621	3.6270	0.4199	−0.2350
S10 2012	0.8277	9.6676	0.3942	−0.0770
A4 1996	1.0868	2.5179	0.4907	−0.3612
A5 1996	1.2087	2.6684	0.4811	−0.3834

Table A3
Acronyms

Acronym	Definition
ADW	Ablation draw wire
AWS	Automatic weather station
IMAU	Institute for Marine and Atmospheric research Utrecht
LHF	Latent heat flux
LW	Longwave radiation
PROMICE	Programme for monitoring of the Greenland Ice Sheet
PTA	Pressure transducer assembly
RCM	Regional climate model
RMS	Centered root-mean-square error
SEB	Surface energy balance
SEC	Sonic eddy covariance
SHF	Sensible heat flux
SMB	Surface mass balance
SR	Sonic height ranger
SW	Shortwave radiation
UAV	Uncrewed aerial vehicle
VPEC	Vertical propeller eddy covariance

Conflict of Interest

The authors declare no conflicts of interest relevant to this study.

Data Availability Statement

The data used in Figures 1, 3, 4 and 6 can be retrieved from Van Tiggelen et al. (2022a). The corrected, 30-min averaged eddy covariance data from the SEC and VPEC stations can be retrieved from Van Tiggelen et al. (2022b). The AWS data at S5 and S6 is available at Smeets et al. (2022). The AWS data at QAS_L and KAN_L is available from Fausto et al. (2022).

Acknowledgments
The authors thank the reviewers for their constructive comments. The authors wish to thank all the persons and institutes that help to maintain the instruments in the field. Giorgio Cover is acknowledged for the help in developing and maintaining the recent eddy covariance stations. Brice Noël is kindly acknowledged for the help with RACMO2.3p2 data. Allan Pedersen, Christopher Shields and Adrien Wehrlé are thanked for their assistance during the yearly maintenance at QAS_L in 2019 and 2020, and the team of Blue Ice Explorer is thanked for the support out of Narsarsuaq. Data from the Programme for Monitoring of the Greenland Ice Sheet (PROMICE) and the Greenland Analogue Project (GAP) were provided by the Geological Survey of Denmark and Greenland (GEUS) at http://www.promice.dk. This work is funded by Utrecht University and by the Netherlands Polar Program (NPP), of the Netherlands Organisation of Scientific Research, section Earth and Life Sciences (NWO/ALWOP.431). This publication was supported by PROTECT. This project has received funding from the European Union's Horizon 2020 research and innovation programme under grant agreement No 869304, PROTECT contribution number 40. This publication was also supported by the Netherlands Earth System Science Centre (NESSC).

References

Agosta, C., Amory, C., Kittel, C., Orsi, A., Favier, V., Gallée, H., et al. (2019). Estimation of the Antarctic surface mass balance using the regional climate model MAR (1979-2015) and identification of dominant processes. *The Cryosphere*, *13*(1), 281–296. https://doi.org/10.5194/tc-13-281-2019

Andreas, E. (1986). A theory for the scalar roughness and the scalar transfer coefficients over snow and sea ice. *Boundary-Layer Meteorology*, *38*(1–2), 159–184. https://doi.org/10.1007/BF00121562

Andreas, E. (2002). Parameterizing scalar transfer over snow and ice: A review. *Journal of Hydrometeorology*, *3*(4), 417–432. https://doi.org/10.1175/1525-7541(2002)003<0417:PSTOSA>2.0.CO;2

Behrens, K. (2021). Radiation sensors. In T. Foken (Ed.), *Springer handbook of atmospheric measurements* (pp. 297–357). Springer International Publishing. https://doi.org/10.1007/978-3-030-52171-4_11

Braithwaite, R. J. (1995). Aerodynamic stability and turbulent sensible-heat flux over a melting ice surface, the Greenland ice sheet. *Journal of Glaciology*, *41*(139), 562–571. https://doi.org/10.3189/S0022143000034882

Brock, B. W., Willis, I. C., & Sharp, M. J. (2006). Measurement and parameterization of aerodynamic roughness length variations at Haut Glacier d'Arolla, Switzerland. *Journal of Glaciology*, *52*(177), 281–297. https://doi.org/10.3189/172756506781828746

Brutsaert, W. (1982). *Evaporation into the atmosphere: Theory, history and applications* (1st ed.). Springer. https://doi.org/10.1007/978-94-017-1497-6

Conway, J. P., & Cullen, N. J. (2013). Constraining turbulent heat flux parameterization over a temperate maritime glacier in New Zealand. *Annals of Glaciology*, *54*(63), 41–51. https://doi.org/10.3189/2013AoG63A604

Elvidge, A. D., Renfrew, I. A., Brooks, I. M., Srivastava, P., Yelland, M., & Prytherch, J. (2021). Surface heat and moisture exchange in the marginal ice zone: Observations and a new parameterization scheme for weather and climate models. *Journal of Geophysical Research: Atmospheres*, *126*(17). https://doi.org/10.1029/2021JD034827

Fausto, R. S., Van As, D., Box, J. E., Colgan, W., Langen, P. L., & Mottram, R. H. (2016). The implication of nonradiative energy fluxes dominating Greenland ice sheet exceptional ablation area surface melt in 2012. *Geophysical Research Letters*, *43*(6), 2649–2658. https://doi.org/10.1002/2016GL067720

Fausto, R. S., Van As, D., & Mankoff, K. D. (2022). AWS one boom tripod v03 [Dataset]. Geological survey of Denmark and Greenland (GEUS). GEUS Dataverse. https://doi.org/10.22008/FK2/8SS7EW

Fausto, R. S., Van As, D., Mankoff, K. D., Vandecrux, B., Citterio, M., Ahlstrøm, A. P., et al. (2021). Programme for monitoring of the Greenland ice sheet (PROMICE) automatic weather station data. *Earth System Science Data*, *13*(8), 3819–3845. https://doi.org/10.5194/essd-13-3819-2021

Fettweis, X., Hofer, S., Krebs-Kanzow, U., Amory, C., Aoki, T., Berends, C., et al. (2020). GrSMBMIP: Intercomparison of the modelled 1980–2012 surface mass balance over the Greenland Ice sheet. *The Cryosphere*, *14*(11), 3935–3958. https://doi.org/10.5194/tc-14-3935-2020

Fitzpatrick, N., Radic, V., & Menounos, B. (2019). A multi-season investigation of glacier surface roughness lengths through in situ and remote observation. *The Cryosphere*, *13*(3), 1051–1071. https://doi.org/10.5194/tc-13-1051-2019

Garbrecht, T., Lüpkes, C., Hartmann, J., & Wolff, M. (2002). Atmospheric drag coefficients over sea ice - Validation of a parameterisation concept. *Tellus Series A Dynamic Meteorology and Oceanography*, *54*(2), 205–219. https://doi.org/10.3402/tellusa.v54i2.12129

Goelzer, H., Nowicki, S., Payne, A., Larour, E., Seroussi, H., Lipscomb, W. H., et al. (2020). The future sea-level contribution of the Greenland ice sheet: A multi-model ensemble study of ISMIP6. *The Cryosphere*, *14*(9), 3071–3096. https://doi.org/10.5194/tc-14-3071-2020

Guo, X., Yang, K., Zhao, L., Yang, W., Li, S., Zhu, M., et al. (2011). Critical evaluation of scalar roughness length parametrizations over a melting valley glacier. *Boundary-Layer Meteorology*, *139*(2), 307–332. https://doi.org/10.1007/s10546-010-9586-9

Hanna, E., Cappelen, J., Fettweis, X., Mernild, S. H., Mote, T. L., Mottram, R., et al. (2021). Greenland surface air temperature changes from 1981 to 2019 and implications for ice-sheet melt and mass-balance change. *International Journal of Climatology*, *41*(S1), E1336–E1352. https://doi.org/10.1002/joc.6771

Hermann, M., Box, J. E., Fausto, R. S., Colgan, W. T., Langen, P. L., Mottram, R., et al. (2018). Application of PROMICE Q-Transect in situ accumulation and ablation measurements (2000-2017) to constrain mass balance at the southern tip of the Greenland ice sheet. *Journal of Geophysical Research: Earth Surface*, *123*(6), 1235–1256. https://doi.org/10.1029/2017JF004408

Herzfeld, U. C., Box, J. E., Steffen, K., Mayer, H., Caine, N., & Losleben, M. V. (2006). A case study or the influence of snow and ice surface roughness on melt energy. *Zeitschrift Gletscherkd. Glazialgeolie*, *39*, 1–42.

Holtslag, A. A. M., & De Bruin, H. A. R. (1988). Applied modeling of the nighttime surface energy balance over land (Vol. *27*). https://doi.org/10.1175/1520-0450(1988)027<0689:amotns>2.0.co;2

Horst, T. W., Semmer, S. R., & Maclean, G. (2015). Correction of a non-orthogonal, three-component sonic anemometer for flow distortion by transducer shadowing. *Boundary-Layer Meteorology*, *155*(3), 371–395. https://doi.org/10.1007/s10546-015-0010-3

Huai, B., Van den Broeke, M. R., & Reijmer, C. (2020). Long-term surface energy balance of the Western Greenland ice sheet and the role of large-scale circulation variability. *The Cryosphere*, *14*(14), 4181–4199. https://doi.org/10.5194/tc-14-4181-2020

IMBIE. (2020). Mass balance of the Greenland ice sheet from 1992 to 2018. *Nature*, *579*(7798), 233–239. https://doi.org/10.1038/s41586-019-1855-2

Jackson, P. (1981). On the displacement height in the logarithmic velocity profile. *Journal of Fluid Mechanics*, *111*(-1), 15–25. https://doi.org/10.1017/s0022112081002279

Jakobs, C. L., Reijmer, C. H., Kuipers Munneke, P., König-Langlo, G., & Van den Broeke, M. R. (2019). Quantifying the snowmelt-albedo feedback at Neumayer station, East Antarctica. *The Cryosphere*, *13*(5), 1473–1485. https://doi.org/10.5194/tc-13-1473-2019

Joffre, S. M. (1988). Modelling the dry deposition velocity of highly soluble gases to the sea surface. *Atmospheric Environment*, *22*(6), 1137–1146. https://doi.org/10.1016/0004-6981(88)90343-5

Kanda, M., Kanega, M., Kawai, T., Moriwaki, R., & Sugawara, H. (2007). Roughness lengths for momentum and heat derived from outdoor urban scale models. *Journal of Applied Meteorology and Climatology*, *46*(7), 1067–1079. https://doi.org/10.1175/JAM2500.1

Kuipers Munneke, P., Smeets, P. C. J. P., Reijmer, C. H., Oerlemans, J., van de Wal, R. S. W., & Van den Broeke, M. R. (2018). The K-transect on the Western Greenland ice sheet: Surface energy balance (2003–2016). *Arctic Antarctic and Alpine Research*, *50*(1), S100003. https://doi.org/10.1080/15230430.2017.1420952

Lenaerts, J. T. M., Smeets, P. C. J. P., Nishimura, K., Eijkelboom, M., Boot, W., van den Broeke, M. R., & van de Berg, W. J. (2014). Drifting snow measurements on the Greenland Ice Sheet and their application for model evaluation. *The Cryosphere*, *8*(2), 801–814. https://doi.org/10.5194/tc-8-801-2014

Li, Q., Bou-Zeid, E., Grimmond, S., Zilitinkevich, S., & Katul, G. (2020). Revisiting the relation between momentum and scalar roughness lengths of urban surfaces. *Quarterly Journal of the Royal Meteorological Society*, *146*(732), 1–31. https://doi.org/10.1002/qj.3839

Mankoff, K., Fettweis, X., Langen, P., Stendel, M., Kjledsen, K., Karlsson, N., et al. (2021). Greenland ice sheet mass balance from 1840 through next week. *Earth System Science Data*, *13*, 5001–5025. https://doi.org/10.5194/essd-13-5001-2021

Mattingly, K. S., Mote, T. L., Fettweis, X., As, D. V., Tricht, K. V., Lhermitte, S., et al. (2020). Strong summer atmospheric rivers trigger Greenland ice sheet melt through spatially varying surface energy balance and cloud regimes. *Journal of Climate*, *33*(16), 6809–6832. https://doi.org/10.1175/JCLI-D-19-0835.1

Moene, A., & van Dam, J. (2014). *Transport in the atmosphere-vegetation-soil continuum*. Cambridge University Press.

Moore, C. J. (1986). Frequency response corrections for eddy correlation systems. *Boundary-Layer Meteorology*, *37*(1–2), 17–35. https://doi.org/10.1007/BF00122754

Noël, B., van de Berg, W. J., Lhermitte, S., & Van den Broeke, M. R. (2019). Rapid ablation zone expansion amplifies north Greenland mass loss. *Science Advances*, *5*(9). https://doi.org/10.1126/sciadv.aaw0123

Nolin, A. W., & Payne, M. C. (2007). Classification of glacier zones in Western Greenland using albedo and surface roughness from the Multi-angle Imaging SpectroRadiometer (MISR). *Remote Sensing of Environment*, *107*(1–2), 264–275. https://doi.org/10.1016/j.rse.2006.11.004

Radic, V., Menounos, B., Shea, J., Fitzpatrick, N., Tessema, M. A., & Déry, S. J. (2017). Evaluation of different methods to model near-surface turbulent fluxes for a mountain glacier in the Cariboo Mountains, BC, Canada. *The Cryosphere*, *11*(6), 2897–2918. https://doi.org/10.5194/tc-11-2897-2017

Raupach, M. R. (1992). Drag and drag partition on rough surfaces. *Boundary-Layer Meteorology*, *60*(4), 375–395. https://doi.org/10.1007/BF00155203

Raupach, M. R. (1994). Simplified expressions for vegetation roughness length and zero-plane displacement as functions of canopy height and area index. *Boundary-Layer Meteorology*, *71*(1–2), 211–216. https://doi.org/10.1007/BF00709229

Reijmer, C., Greuell, W., & Oerlemans, J. (1999). The annual cycle of meteorological variables and the surface energy balance on Berkner Island, Antarctica. *Annals of Glaciology*, *29*, 49–54. https://doi.org/10.3189/172756499781821166

Schotanus, P., Nieuwstadt, F. T., & De Bruin, H. A. (1983). Temperature measurement with a sonic anemometer and its application to heat and moisture fluxes. *Boundary-Layer Meteorology*, *26*(1), 81–93. https://doi.org/10.1007/BF00164332

Shao, Y., & Yang, Y. (2008). A theory for drag partition over rough surfaces. *Journal of Geophysical Research: Earth Surface*, *113*(2), 1–9. https://doi.org/10.1029/2007JF000791

Sicart, J. E., Litt, M., Helgason, W., Ben Tahar, V., & Chaperon, T. (2014). A study of the atmospheric surface layer and roughness lengths on the high-altitude tropical Zongo glacier, Bolivia. *Journal of Geophysical Research: Atmospheres*, *119*, 3793–3808. https://doi.org/10.1002/2013JD020615

Smeets, P. C. J. P., van den Broeke, M. R., Boot, W., Cover, G., Eijkelboom, M., Greuell, W., et al. (2022). Automatic weather station collected from 2003 to 2021 at the Greenland ice sheet along the K-transect, West-Greenland [Dataset]. PANGAEA. https://doi.org/10.1594/PANGAEA.947483

Smeets, P. C. J. P., Kuipers Munneke, P., van As, D., Van den Broeke, M. R., Boot, W., Oerlemans, H., et al. (2018). The K-transect in west Greenland: Automatic weather station data (1993–2016). *Arctic Antarctic and Alpine Research*, *50*(1). https://doi.org/10.1080/15230430.2017.1420954

Smeets, P. C. J. P., & Van den Broeke, M. R. (2008a). Temporal and spatial variations of the aerodynamic roughness length in the ablation zone of the Greenland ice sheet. *Boundary-Layer Meteorology*, *128*(3), 315–338. https://doi.org/10.1007/s10546-008-9291-0

Smeets, P. C. J. P., & Van den Broeke, M. R. (2008b). The parameterisation of scalar transfer over rough ice. *Boundary-Layer Meteorology*, *128*(3), 339–355. https://doi.org/10.1007/s10546-008-9292-z

Smith, M. W., Quincey, D. J., Dixon, T., Bingham, R. G., Carrivick, J. L., Irvine-Fynn, T. D. L., & Rippin, D. M. (2016). Aerodynamic roughness of glacial ice surfaces derived from high-resolution topographic data. *J. Geophys. Res.Earth Surface*, *121*(4), 748–766. https://doi.org/10.1002/2015JF003759

Steffen, K. (1995). Surface energy exchange during the onset of melt at the equilibrium line altitude of the Greenland ice sheet. *Annals of Glaciology*, *21*, 13–18. https://doi.org/10.3189/s0260305500015536

Van den Broeke, M. R., Enderlin, E. M., Howat, I. M., Kuipers Munneke, P., Noël, B. P., van De Berg, W. J., et al. (2016). On the recent contribution of the Greenland ice sheet to sea level change. *The Cryosphere*, *10*(5), 1933–1946. https://doi.org/10.5194/tc-10-1933-2016

Van den Broeke, M. R., Smeets, P. C. J. P., Ettema, J., Van Der Veen, C., Van De Wal, R., & Oerlemans, J. (2008). Partitioning of melt energy and meltwater fluxes in the ablation zone of the west Greenland ice sheet. *The Cryosphere*, *2*(2), 179–189. https://doi.org/10.5194/tc-2-179-2008

Van den Broeke, M. R., Smeets, P. C. J. P., & van de Wal, R. S. W. (2011). The seasonal cycle and interannual variability of surface energy balance and melt in the ablation zone of the west Greenland ice sheet. *The Cryosphere*, *5*(2), 377–390. https://doi.org/10.5194/tc-5-377-2011

Van den Broeke, M. R., van As, D., Reijmer, C., & van de Wal, R. (2004). Assessing and improving the quality of unattended radiation observations in Antarctica. *Journal of Atmospheric and Oceanic Technology*, *21*(9), 1417–1431. https://doi.org/10.1175/1520-0426(2004)021<1417:AAITQO>2.0.CO;2

Van Tiggelen, M., Smeets, P. C., Reijmer, C. H., van den Broeke, M. R., van As, D., Box, J. E., & Fausto, R. S. (2022a). Dataset for figures [Dataset]. Institute for Marine and Atmospheric research Utrecht (IMAU). Zenodo. https://doi.org/10.5281/zenodo.6382815

Van Tiggelen, M., Smeets, P. C., Reijmer, C. H., & Van den Broeke, M. R. (2020). A vertical propeller eddy-covariance method and its application to long-term monitoring of surface turbulent fluxes on the Greenland ice sheet. *Boundary-Layer Meteorology*, *176*(3), 441–463. https://doi.org/10.1007/s10546-020-00536-7

Van Tiggelen, M., Smeets, P. C., Reijmer, C. H., Wouters, B., Steiner, J. F., Nieuwstraten, E. J., et al. (2021). Mapping the aerodynamic roughness of the Greenland ice sheet surface using ICESat-2: Evaluation over the K-transect. *The Cryosphere*, *15*(6), 2601–2621. https://doi.org/10.5194/tc-15-2601-2021

Van Tiggelen, M., Smeets, P. C. J. P., Reijmer, C. H., van den Broeke, M. R., van As, D., Box, J. E., & Fausto, R. S. (2022b). Eddy-covariance measurements over the Greenland ice sheet (K-transect & Q-transect) and Iceland (Vatnajökull) [Dataset]. Institute for Marine and Atmospheric research Utrecht (IMAU). PANGAEA. https://doi.org/10.1594/PANGAEA.945307

Wang, W., Zender, C. S., As, D. V., Fausto, R. S., & Laffin, M. K. (2021). Greenland surface melt dominated by solar and sensible heating. *Geophysical Research Letters*, *48*(7), 1–16. https://doi.org/10.1029/2020GL090653

Webb, E. K., Pearman, G., & Leuning, R. (1980). Correction of flux measurements for density effects due to heat and water vapour transfer. *Quarterly Journal of the Royal Meteorological Society*, *106*(447), 85–100. https://doi.org/10.1002/qj.49710644707